In-situ alloying of stainless steel 316L by co-inoculation of Ti and Mn using LPBF additive manufacturing: Microstructural evolution and mechanical properties

In-situ alloying of stainless steel 316L by co-inoculation of Ti and Mn using LPBF additive manufacturing: microstructural evolution and mechanical properties

Mohammad Reza Jandaghi [*,1], Hesam Pouraliakbar [2], Sang Hun Shim [3], Vahid Fallah [2], Sun Ig Hong [3], Matteo Pavese [1]

[1] *Department of Applied Science and Technology, Politecnico di Torino, Corso Duca Degli Abruzzi 24, 10129 Torino, Italy*

[2] *Azar Advanced Manufacturing Laboratory (AAML), Department of Mechanical and Materials Engineering, Queen's University, Kingston, ON K7L 3N6, Canada*

[3] *Department of Materials Science and Engineering, Chungnam National University, Daejeon 34134, Republic of Korea*

Corresponding author**; E-mail: **mohammadreza.jandaghi@polito.it

DOI: https://doi.org/10.1016/j.msea.2022.144114

Abstract

The grain refining impact of Ti in additively manufactured steels as well as the outstanding formability of high-Mn steels owing to their low stacking fault energy (SFE) has been confirmed in the literature. In the current work, Ti and Mn were inoculated simultaneously to the stainless steel 316L by laser powder bed fusion (LPBF) in-situ alloying. The local accumulation of the additions developed complexes of Ti-rich brittle phases that improved strength. Microstructural observations revealed the formation of intermetallic chunks of FeTi (*bcc*), *σ* (*tetragonal*), and C14 Laves phase (*hcp*) surrounded by emerged ferrite grains within the austenite. The rapid solidification of the molten tracks induced significant thermal stresses, which were responded by the generation of geometrically necessary dislocations (GNDs) at the austenite/ferrite interfaces, and activation of synchroshear mechanism within the Laves phase along with thermally activated slip systems in FeTi phase. Mn addition contributed to higher interface cohesion by facilitating dissociation of dislocations.

Keywords: *Additive Manufacturing; In-situ alloying; Grain refinement; Deformation mechanism; Intermetallics; Microstructure; Mechanical properties.*

1. Introduction

Thanks to advantages such as building near-net-shape components with superior mechanical properties due to intrinsic high cooling rate, additive manufacturing (AM) is growingly replacing the conventional production methods **[1]**. Among the different AM techniques, laser powder bed fusion (LPBF) is one of the most promising ones for manufacturing metallic parts through layer-by-layer fusion and consolidation of powder feedstock according to a computer-aided design (CAD) **[2]**.

Compared to the other additive manufacturing methods like electron beam melting (EBM), direct energy deposition (DED), wire arc additive manufacturing (WAAM), and laser metal deposition (LMD), LPBF has higher dimensional precise and lower surface roughness. However, the building rate of the LPBF is lower than the other counterparts **[3]**. The elemental ratio of the powders used for LPBF is usually adjusted by pre-alloying. However, the substitution of the pre-alloying steps comprising casting and atomization by in-situ alloying would save time and cost and, in turn, can increase the productivity of AM methods. Inhomogeneous dispersion, evaporation, and incomplete melting of the guest elements are the main challenges for AM in-situ alloying **[4]**. Hence, incorporating elements of comparable melting points would provide a more reliable feedstock for production. Many researchers exploited in-situ alloying as a low-cost strategy for structural modification **[5]**, particularly grain refinement **[6]**. So far, several solute elements for grain refining in different alloying systems have been introduced **[7]**. The refinement mechanism of the inoculants can be assorted into two main categories: (1) by affecting the growth restriction factor and changing the heat flow direction (e.g., Cu in Ti alloys **[8]**), and (2) by reacting with the matrix to form the phases that can pin the grain boundaries (for instance, Zr **[9]** and Sc **[10]** in Al alloys and Ni **[11]** and La **[12]** in Ti alloys). Recent studies on inoculating steels using pure Ti **[13]** and its compounds (such as TiN) **[14]** revealed that the formation of nano-oxides in the melt pool can hinder the epitaxial growth of grains and typical severe texturing in AM. Additionally, it has been confirmed that raising the Mn content in steels would reduce the stacking fault energy (SFE) and can activate the twinning mode besides the slip systems during plastic deformation **[15]**. SS316L has excellent corrosion resistance and biocompatibility **[16]**. Nevertheless, its low yield strength at room temperature would make some complications for using them in extreme environments. Therefore, the development of high-strength stainless steel has been of great interest **[17]**. This study aimed to benefit from the simultaneous inoculation of Ti and Mn and their synergistic potential in the strengthening and work-hardening of SS316L steel fabricated by the LPBF technique.

2. Experimental methods

Commercial gas atomized SS316L powder (Höganäs, Sweden) (particle size: 15-50 μm) was blended with 1 wt.% Ti (Sigma Aldrich, Germany) (particle size: 15-45 μm) and 2 wt.% Mn (Sigma Aldrich, Germany) (particle size: 5-30 μm) and used as feedstock material. A Sharebot METALONE Laser with a spot size of 40 μm was employed to print the specimens under an argon atmosphere (O_2<100 ppm) with the optimized process parameters of 90 W, 400 mm/s, 30 μm layer thickness, 70 μm hatch spacing, and 67° scan rotation between layers (i.e., the set of parameters that obtained the highest relative density). Samples were printed on an SS304L substrate with distinct geometries of (1) cubic samples with a dimension of 10×10×10 mm^3 for microstructural investigations and (2) tensile bars

with a gauge dimension of 32×6×4 mm^3 according to the ASTM-E8 sub-size standard. Room-temperature quasi-static tensile tests were conducted using a Zwick/Roell Z050 machine at starting strain rate of 2×10^{-3}/s. The microhardness measurement was executed using a VMHT machine with an applied load of 0.1 kg and a dwell time of 15 s. For metallography, mirror polished specimens were chemically etched by a mixed solution of 15HCl:10HNO3:1CH3COOH for 10 s. Microstructural characterizations were performed using a DSX1000 Digital OM and a JEOL JSM7001F field emission scanning electron microscope (FE-SEM) equipped with an electron backscatter diffraction (EBSD) detector. The acquired EBSD data were analyzed using EDAX OIM Analysis™ software. TEM analysis was carried out on FIB-cut thin foils using a dual-beam FEI Helios-NanoLab FIB and JEOL JEM-2100F TEM operated at 200 kV. Lattice transformations were recorded by an X-Pert Philips x-ray diffractometer (XRD).

3. Results and discussions

The optical microscopy (OM), SEM, and EBSD micrographs of the as-built SS316L and reinforced samples are presented in **Fig. 1**. As can be seen, despite applying the optimized parameters, the guest elements have not been uniformly distributed inside the austenitic matrix. The OM images (**Fig. 1(a** vs. **f)**) and EBSD IPFs (**Fig. 1(b** vs. **g)**) reveal the formation of a bimodal structure in the reinforced sample, i.e., comprising ultrafine grains around the stacked phases and coarse columnar grains at regions far from the generated phases (indicating the epitaxial growth), as opposed to a predominantly columnar structure in the unreinforced sample. According to the SEM micrograph of **Fig. 1(h)**, the phases are mostly formed at the melt pool boundaries as well as vast areas inside some melt pools. The formation of new phases limited the growth of the typical cellular structure of AMed SS316L. Likewise, the intensive vulnerability of these phases in corrosive etchant (white districts in SEM images) arises from their chemical composition difference. Analysis of the acquired phase maps revealed that alloying elements in the austenitic matrix formed some unconventional *bcc* and *hcp* phases (comparing **Fig. 1(d** vs. **i)**). The partial refinement of the grains besides the formation of new phases that hindered the epitaxial growth of the columnar grains attenuated the typical texturing along the buildup direction in AMed alloy. This can be inferred from a more randomized distribution of grains' orientation depicted in the pole figures (PFs) shown in **Fig. 1(e** vs. **j)**. Prior works have demonstrated that inoculated Ti in SS316L **[18]** and SS316L in Ti6Al4V **[19]** by in-situ alloying exhibit a non-uniform distribution and create similar accumulated regions. Though the grain refinement impact of SS316L in Ti6Al4V, and formed TiO nanoparticles in SS316L alloys have already been highlighted and studied, several substantial points remain unexplored. Accumulation of inoculated elements occurs at the expense of depletion of other regions and, eventually, localized concentrations of the elements lead to the advent of unfavorable phases which may degrade the properties.

Fig. 2(a) displays the representative tensile stress-strain curves and the corresponding fracture surfaces of the AMed SS316L specimens. Although the average yield strength (YS) (484±14 vs. 532±20 MPa) and ultimate strength (UTS) (602±17 vs. 648±22 MPa) of the reinforced sample were higher, the formation of new phases significantly deteriorated the mean elongation to failure (25.3±1.4% vs. 11.2±1%) and resulted in a higher fraction of brittle failure. A similar trend was repeated by several tensile examinations. The difference in fracture behavior is readily conceivable from the fracture surface of the unreinforced specimen mostly covered with dimples, as opposed to cleavage surfaces for the reinforced specimen. From **Fig 2(a)**, ruptured areas showed Fe_2Ti indication with higher Ni and a lower Cr content than the typical composition of SS316L alloy. **Fig. 2(b)** illustrates the true stress-strain curves for the representative samples and the evolution of work-hardening rates for the examined tensile samples. In stage II of the reinforced sample, the dominancy of brittle phases and the prevention of dislocations' glide caused a limited slip and steeper declining work-hardening rate eventuated in confined plastic deformation. Subsequently, an early failure led to a limited post-necking elongation, i.e., by the acceleration of microcracks growth and dimples coalescence, resulting in a shortened stage III.

According to the microhardness variation profile in **Fig. 2(c)** and corresponding OM micrographs of the examined regions, the reinforced sample displayed local hardness values of about two times greater than values for the unreinforced sample when the indenter passes through the brittle phases. Zhai et al. **[18]** observed similar phase accumulation zones and attributed the superior hardness of those regions to the local segregation of Ti. The STEM image of **Fig. 3(a)** is provided from a melt pool boundary that is enriched by the accumulated phases. As can be inferred from the elemental distribution maps in **Fig. 3(b)**, the TEM image in **Fig. 3(c)** and its corresponding SAED patterns, the inoculation of Ti, has led to its aggregation and a local Ti/Fe ratio enhancement; therefore, FeTi has been formed within the region of stacked phases (as labeled in **Fig. 3(a)**) with a superlattice *bcc* reflection (**Fig. 3(c_1)**).

XRD patterns of **Fig. 3(d)** validated the existence of the *bcc* phase in the reinforced sample. SAED patterns (**Fig. 3(c_2)** proved that the FeTi chunks are surrounded by the C14 Laves phase with an *hcp* structure containing lower Ti and higher Cr and Mn contents (as can be inferred from the EDS maps in **Fig. 3(b)**). Since Ti is a ferrite stabilizer element, a *bcc* ferritic interlayer is formed between the intermetallics (FeTi/Laves phase) and the *fcc* austenitic matrix. The ferrite grains contained higher Cr and lower Ni and Ti values compared to its neighboring Laves phase (following the EDS maps in **Fig. 3(b)**). Rapid solidification of the deposited layers left substantial residual stress in the austenitic zone which was responded by the generation of a large number density of GNDs at the austenitic/ferritic interface (**Fig. 3(c)**). The strain gradient between the hard intermetallics and austenitic matrix led to GNDs pilling up at the interface within the softer phase **[20]**. Likewise, the EDS map of Ni reveals a Ni-

rich branched matrix in between the FeTi chunks and Laves phase. Due to XRD limitation in recording the diffraction of phases with lower volume fractions, Laves phase, and other emerged phases except for bcc and fcc ones are not detected in the obtained patterns.

The line scans and EDS maps (**Fig. 4(a)**) obtained from the branched matrix proved that these zones were enriched in Cr, Ni, and Mn and depleted in Ti. The SAED pattern of the detected phase in **Fig. 4(b)** exhibits lattice constants like those of a typical σ phase with a tetragonal crystal structure (some reported constants from the literature are tabulated in **Fig. 4(d)**). The lattice parameters for the σ phase based on the obtained SAED pattern (**Fig. 4(b)**) are a=8.929 Å and c=4.549 Å. Lee et al. **[21]** have examined the Mn variation on precipitation behavior of the *σ* phase in austenitic steels and found that Mn can replace Mo within its structure. Also, it has been proven that the addition of ferrite stabilizer elements (such as Cr, Mo, and Ti) instantly forms the *σ* phase **[22]**. Therefore, Mn addition can adversely impact formability by reacting with Cr and Ni to develop an undesirable *σ* phase. From **Fig. 4(b)** and **Fig. 4(c)**, some TiO nanoparticles are formed and observable inside the ferrite interlayers, FeTi, and Laves phases (fine black dots in **Fig. 3(a)** and **4(a)**). These particles have been introduced as the major grain refiners in Ti-reinforced steels **[18]**.

Although TiO nanoparticles have not preferentially settled at the grain boundaries to pin them, as can be seen in **Fig. 4(b)**, they will act as an obstacle against dislocations motion and, therefore, enhance the tensile strength of the reinforced sample **[23]**. The Cr-containing silicates are the most prevalent oxides in SS316L alloy. These inclusions are a constituent part of the feedstock particles and often dissociate and reform during the printing of stainless steel **[24]**. Compared to the titanium oxides, the formation enthalpy of the silicates is substantially lower **[25]**. So, thermodynamically, silicon oxides are more favorable, and the formation of TiO nanoparticles may be due to the higher kinetics of Ti and oxygen reaction and localized segregation and availability of enough Ti atoms, given the ultrafast cooling rates during LPBF.

Fig. 5(a) depicts an overview of microstructural evolution from the boundary toward the center of a melt pool including complex regions formed due to Ti and Mn accumulation. As can be seen in the top-right corner, the FeTi phase and adjacent Laves phase have no distinguishable boundaries. Also, comparing **Fig. 5(b)** and the obtained chemical compositions (given in **Fig. 5(e)**), illuminate that the Laves phases formed between the ferrite grains and FeTi phase exhibit two distinct morphologies and compositions. The Laves phase closer to the melt pool center contains higher Ti and lower Cr contents than the one beside the ferrite grains. This phase appears to have responded to thermal stresses during rapid solidification of the melt pool by activating the synchroshear mechanism, as can be inferred from **Figs. 5(c** and **d)**. Owing to the low activation energy, synchroshear is the most prevalent mechanism for the basal slip in the Laves phase with *hcp* crystallography **[26].** Indeed, the twin-like structures in **Fig. 5(d)** are formed by multiple synchroshears and acted as slip planes in the structure

of the Laves phase under the applied thermal stresses. The magnitude of synchronous glide of partial dislocations on adjacent parallel atomic planes is equal to the length of Burgers vector **[27]**. As depicted in the SAED pattern of **Fig. 3**, FeTi has a superlattice *bcc* structure and the slip systems in *bcc* require sufficient heat to activate. During solidification, the synergetic effect of activation of slip systems in FeTi and the decreased SFE by Mn addition (which facilitates the dissociation of dislocations), generated numerous statistically stored dislocations (SSDs). It could be inferred that the absence of interface microcracks in the presence of brittle phases (i.e., intermetallic) denotes higher interface cohesion which can be in direct correlation with the feasibility of dislocations dissociation by Mn addition. Hence, the stacked phases in the center of the melt pools are recognizable from their morphology; i.e., the regions with highly accumulated dislocations contain the FeTi phase, whereas the smooth phases containing twin-like structures represent the Laves phase. Compared to SSDs, GNDs are more effective in the improvement of work hardening and mechanical strength of the alloys **[28]**. It has been revealed that having the same dislocation density, the yield stress and work hardening of the high-GND steels will be much higher than high-SSD ones due to the higher heterogeneous deformation-induced strengthening. However, the role of GNDs is more highlighted in the early stage of work hardening, where the plastic strain is small, but SSDs dominate in the later stages where the strain is significant **[26]**.

4. Conclusion

In the present work, to exploit the refinement and strengthening effect of Ti and SFE reducing impact of Mn, they were inoculated to SS316L simultaneously by laser powder bed fusion (LPBF) in-situ alloying. Nonuniform distribution of the additives eventuated in the formation of complex intermetallics while rapid solidification led to a higher mechanical strength, culminating in early failure of the reinforced sample. In-depth microstructural analysis revealed that stacked phases, consisting of FeTi (*bcc*) and two different C14 Laves phases (*hcp*), were surrounded by ferrite interlayers within the austenitic matrix. Development of σ phase beside Laves phase and dispersion of fine TiO nanoparticles inside the emerged phases were also detected. Rapid solidification induced large thermal stresses that were responded by the generation of geometrically necessary dislocations (GNDs) at the austenite/ferrite interface and activation of synchroshear mechanism and thermally-activated slip systems in Laves phase and FeTi, respectively.

References

[1] H. Qin, Q. Dong, V. Fallah, M.R. Daymond, Rapid Solidification and Non-equilibrium Phase Constitution in Laser Powder Bed Fusion (LPBF) of AlSi10Mg Alloy: Analysis of Nano-precipitates, Eutectic Phases, and Hardness Evolution, Metallurgical and Materials Transactions A 51(1) (2020) 448-466.

[2] L. Cui, F. Jiang, D. Deng, T. Xin, X. Sun, R.T. Mousavian, R.L. Peng, Z. Yang, J. Moverare, Cyclic response of additive manufactured 316L stainless steel: The role of cell structures, Scripta Materialia 205 (2021) 114190.
[3] A. Garcia-Colomo, D. Wood, F. Martin, S.W. Williams, A comparison framework to support the selection of the best additive manufacturing process for specific aerospace applications, (2019).
[4] M.R. Jandaghi, A. Aversa, D. Manfredi, F. Calignano, L. Lavagna, M. Pavese, In situ alloying of AlSi10Mg-5 wt% Ni through laser powder bed fusion and subsequent heat treatment, Journal of Alloys and Compounds 904 (2022) 164081.
[5] M.R. Jandaghi, H. Pouraliakbar, V. Fallah, E. Ghassemali, A. Saboori, M. Pavese, Additive manufacturing of nano-oxide decorated AlSi10Mg composites: A comparative study on Gd2O3 and Er2O3 additions, Materials Characterization (2022) 112206.
[6] D. Zhang, A. Prasad, M.J. Bermingham, C.J. Todaro, M.J. Benoit, M.N. Patel, D. Qiu, D.H. StJohn, M. Qian, M.A. Easton, Grain refinement of alloys in fusion-based additive manufacturing processes, Metallurgical and Materials Transactions A 51(9) (2020) 4341-4359.
[7] H. Ikehata, E. Jägle, Evaluation of microstructure and tensile properties of grain-refined, Ti-alloyed ferritic stainless steel fabricated by laser powder bed fusion, Materials Science and Engineering: A 818 (2021) 141365.
[8] D. Zhang, D. Qiu, M.A. Gibson, Y. Zheng, H.L. Fraser, D.H. StJohn, M.A. Easton, Additive manufacturing of ultrafine-grained high-strength titanium alloys, Nature 576(7785) (2019) 91-95.
[9] Y. Guo, W. Wei, W. Shi, B. Zhang, X. Zhou, S. Wen, X. Wu, K. Gao, L. Rong, H. Huang, Effect of Er and Zr additions and aging treatment on grain refinement of aluminum alloy fabricated by laser powder bed fusion, Journal of Alloys and Compounds 912 (2022) 165237.
[10] Q. Jia, P. Rometsch, P. Kürnsteiner, Q. Chao, A. Huang, M. Weyland, L. Bourgeois, X. Wu, Selective laser melting of a high strength AlMnSc alloy: Alloy design and strengthening mechanisms, Acta Materialia 171 (2019) 108-118.
[11] Z. Xiong, X. Pang, S. Liu, Z. Li, R. Misra, Hierarchical refinement of nickel-microalloyed titanium during additive manufacturing, Scripta Materialia 195 (2021) 113727.
[12] P. Barriobero-Vila, J. Gussone, A. Stark, N. Schell, J. Haubrich, G. Requena, Peritectic titanium alloys for 3D printing, Nature communications 9(1) (2018) 1-9.
[13] H. Ikehata, D. Mayweg, E. Jaegle, Grain refinement of Fe--Ti alloys fabricated by laser powder bed fusion, Materials & Design 204 (2021) 109665.
[14] A. Durga, N.H. Pettersson, S.B.A. Malladi, Z. Chen, S. Guo, L. Nyborg, G. Lindwall, Grain refinement in additively manufactured ferritic stainless steel by in situ inoculation using pre-alloyed powder, Scripta Materialia 194 (2021) 113690.
[15] W.-L. Jin, J.-L. Cao, J.-X. Li, Combined Effects of Mn, C, and H on the Stacking Fault Energy in Austenitic Mn Steels, steel research international 92(7) (2021) 2000550.
[16] M. Jandaghi, A. Saboori, L. Iuliano, M. Pavese, On the effect of rapid annealing on the microstructure and mechanical behavior of additively manufactured stainless steel by Laser Powder Bed Fusion, Materials Science and Engineering: A 828 (2021) 142109.
[17] Y.-K. Kim, K.-A. Lee, Direct energy deposition of high strength austenitic stainless steel matrix nanocomposite with superior ductility: Microstructure, tensile properties, and deformation behavior, Materials Characterization 179 (2021) 111358.
[18] W. Zhai, W. Zhou, S.M.L. Nai, Grain refinement of 316L stainless steel through in-situ alloying with Ti in additive manufacturing, Materials Science and Engineering: A 840 (2022) 142912.
[19] T. Zhang, Z. Huang, T. Yang, H. Kong, J. Luan, A. Wang, D. Wang, W. Kuo, Y. Wang, C.-T. Liu, In situ design of advanced titanium alloy with concentration modulations by additive manufacturing, Science 374(6566) (2021) 478-482.
[20] T. Jing, H. Zheng, Q. Liao, L. Song, H. Peng, Y. Wen, Homogeneously introducing more and thinner nanotwins by engineering annealing twin boundaries: A TWIP steel as an example, Materials Science and Engineering: A 840 (2022) 142908.
[21] C. Lee, Y. Lee, C. Lee, S. Hong, Precipitation behavior of the sigma phase with Ni and Mn content variations in superaustenitic stainless steel weld metal, Materials Characterization 144 (2018) 148-154.

[22] C.-C. Hsieh, W. Wu, Overview of Intermetallic Sigma (?) Phase Precipitation in Stainless Steels, ISRN Metallurgy 2012 (2012).
[23] Y.M. Wang, T. Voisin, J.T. McKeown, J. Ye, N.P. Calta, Z. Li, Z. Zeng, Y. Zhang, W. Chen, T.T. Roehling, Additively manufactured hierarchical stainless steels with high strength and ductility, Nature materials 17(1) (2018) 63-71.
[24] P. Deng, M. Karadge, R.B. Rebak, V.K. Gupta, B.C. Prorok, X. Lou, The origin and formation of oxygen inclusions in austenitic stainless steels manufactured by laser powder bed fusion, Additive Manufacturing 35 (2020) 101334.
[25] T.V. Charlu, O.J. Kleppa, T.B. Reed, High-temperature combustion calorimetry III. Enthalpies of formation of titanium oxides, The Journal of Chemical Thermodynamics 6(11) (1974) 1065-1074.
[26] K. Xiang, L. Ding, Z. Jia, X. Yang, Q. Liu, Z. Hao, Phase transition induced by synchroshear in Al-Zn-Mg-Cu alloy, Scripta Materialia 212 (2022) 114577.
[27] J. Guénolé, F.-Z. Mouhib, L. Huber, B. Grabowski, S. Korte-Kerzel, Basal slip in Laves phases: The synchroshear dislocation, Scripta Materialia 166 (2019) 134-138.
[28] N. Wang, Y. Chen, G. Wu, Q. Zhao, Z. Zhang, L. Zhu, J. Luo, Non-equivalence contribution of geometrically necessary dislocation and statistically stored dislocation in work-hardened metals, Materials Science and Engineering: A 836 (2022) 142728.

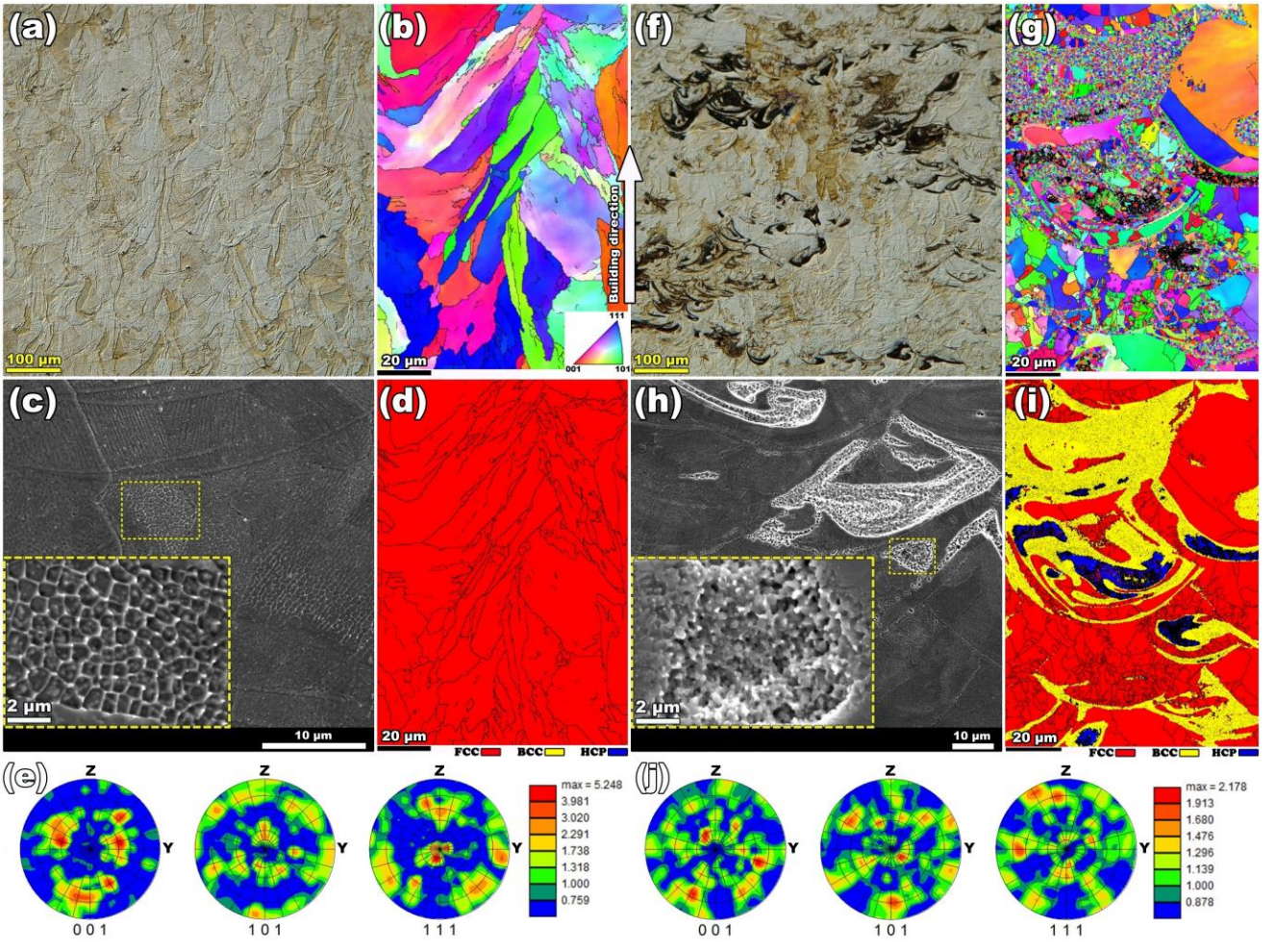

Fig. 1. OM micrographs, EBSD IPFs, SEM images, phase maps, and PFs of (a-e) unreinforced and (f-j) reinforced AMed SS316L alloys.

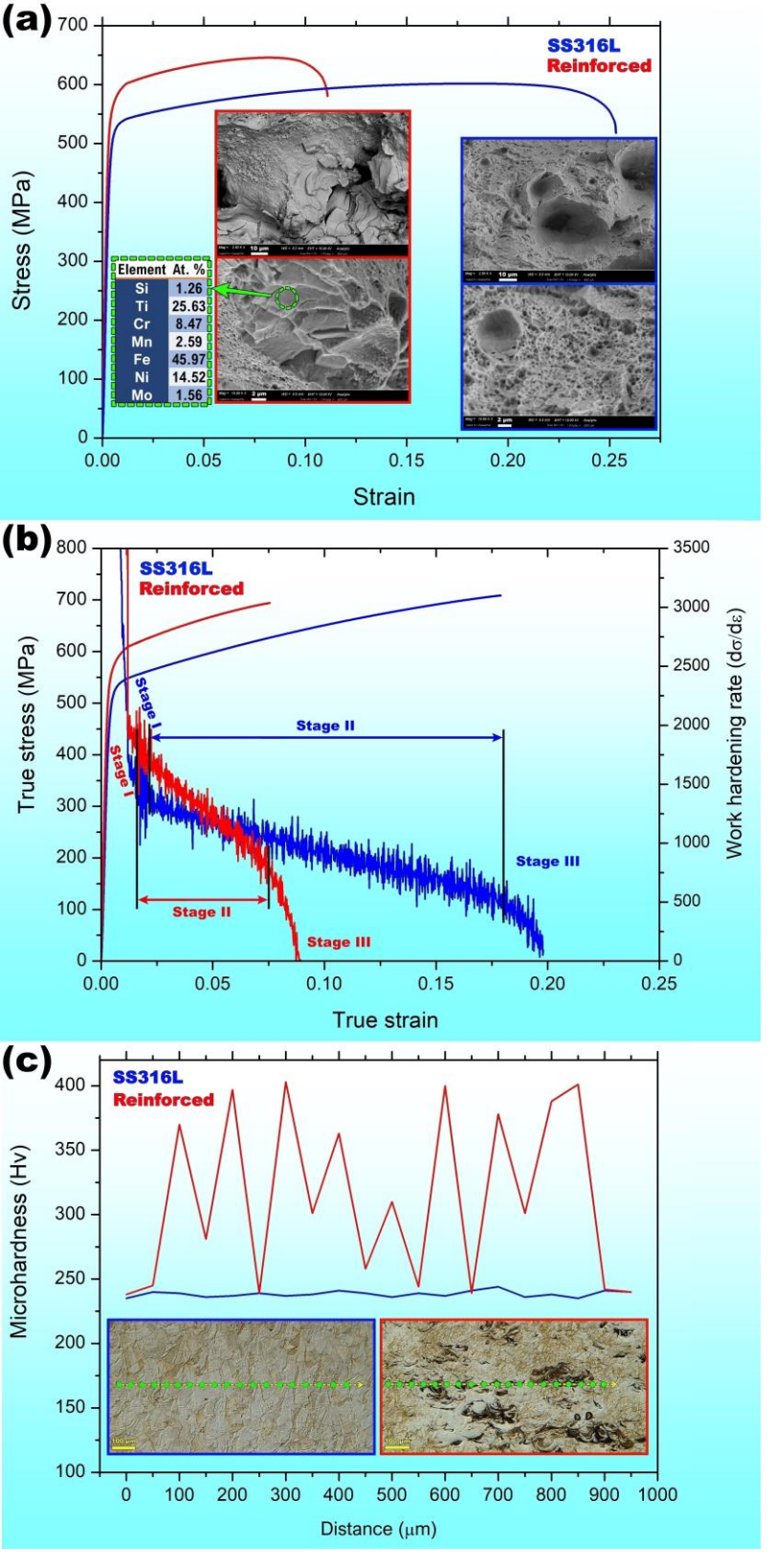

Fig. 2. Representative tensile engineering stress-strain curves and corresponding fracture surfaces (a), true stress-strain curves and evolution of work-hardening rates (b), and microhardness profiles (c) of AMed SS316L alloys.

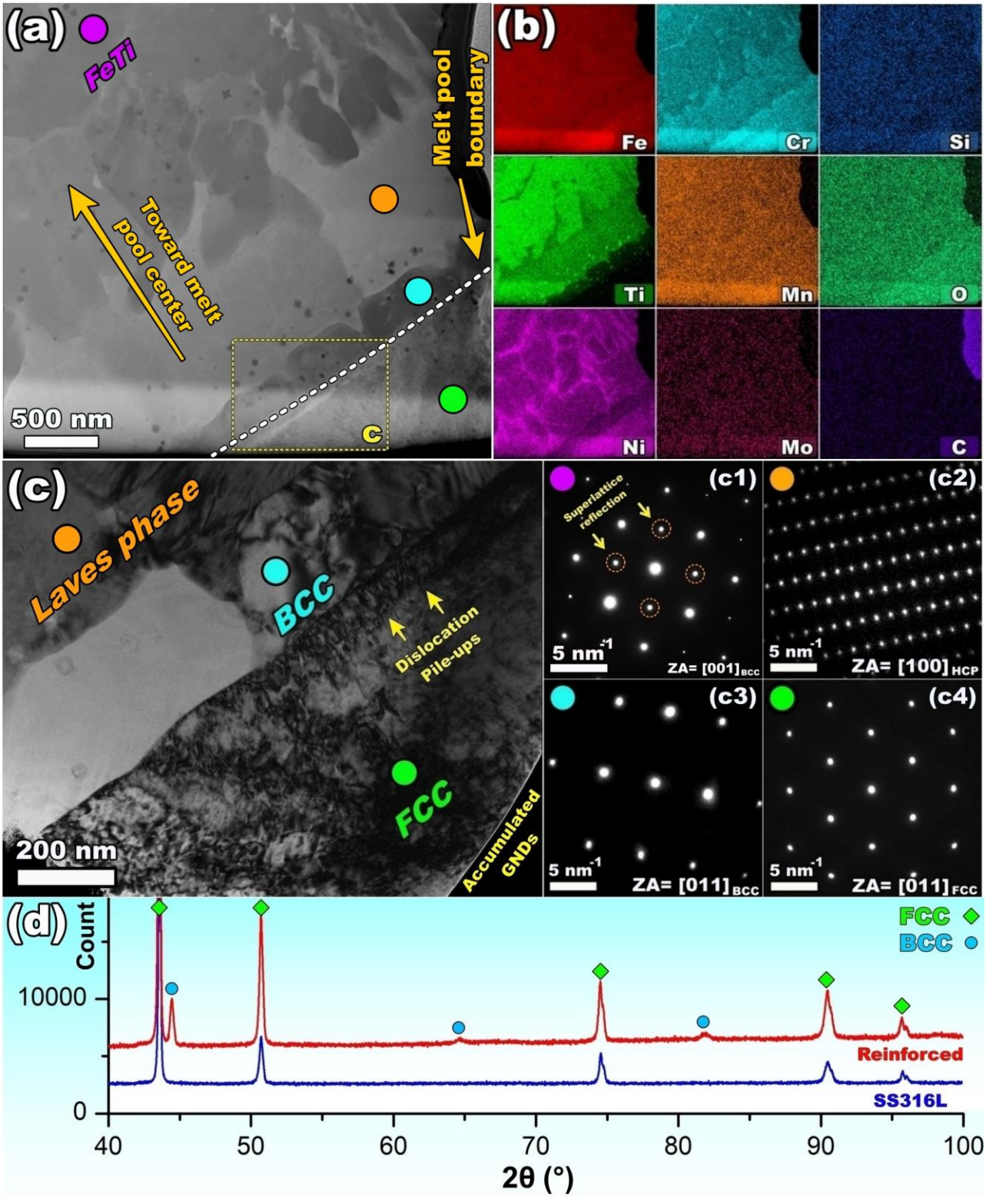

Fig. 3. (a) STEM image obtained from the interface of stacked phases and austenitic matrix, (b) corresponding EDS elemental maps, (c) TEM image and SAED patterns of different regions of the reinforced sample, and (d) recorded XRD patterns for the AMed SS316L alloys.

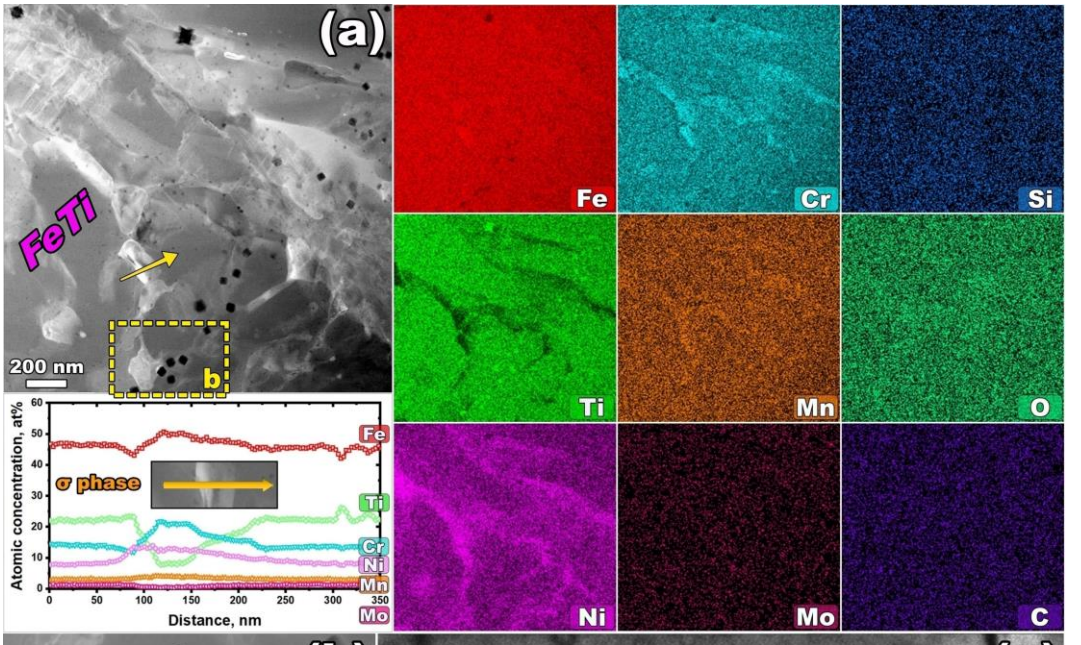

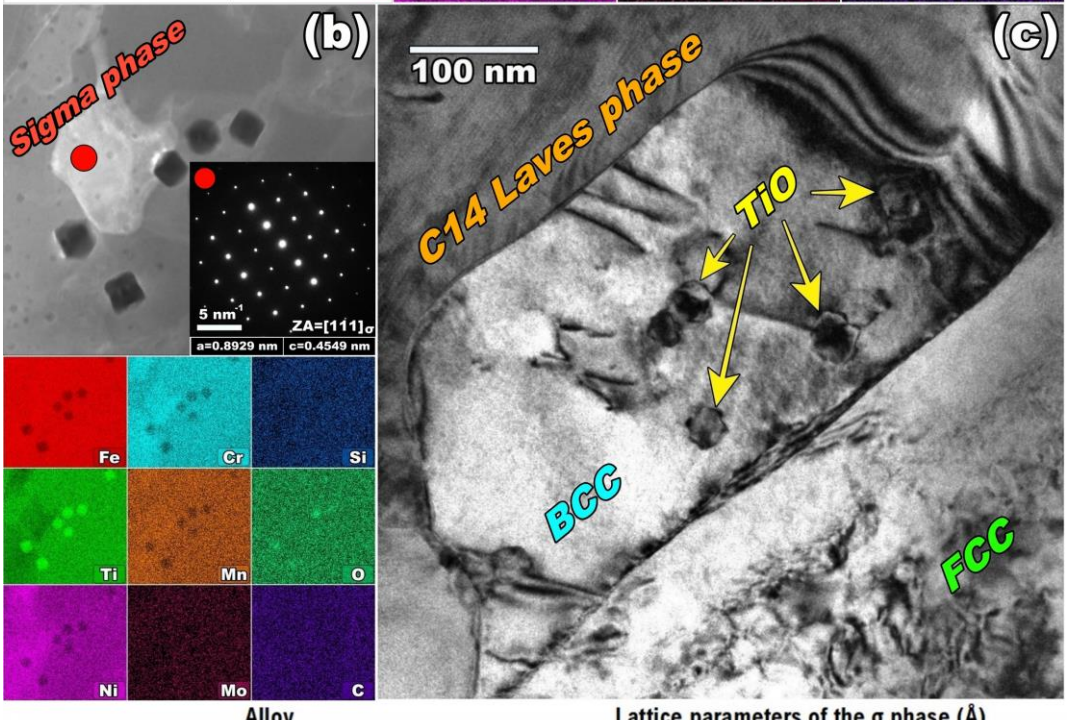

(d)

Alloy	Lattice parameters of the σ phase (Å)
Reinforced SS316L by Ti and Mn (This work)	a = 8.929, c = 4.549
Fe-Cr	a = 8.799, c = 4.544
Fe-Mo	a = 9.188, c = 4.812
Steel 316	a = 8.28~8.38, c = 4.597~4.599
Steel 316L	a = 9.21, c = 4.78
20Cr-25-34Ni-6.5-8Mo	a = 8.87, c = 4.61

Fig. 4. (a) STEM image, EDS line scans, and corresponding EDS maps acquired from the branched matrix, (b) TEM image and corresponding EDS maps along with SAED pattern

exhibiting the formation of the TiO nanoparticles and σ phase, (c) TEM image illustrating the magnified view of TiO nanoparticles embedded in a ferrite grain and (d) collected lattice parameters of σ phase from the literature [22].

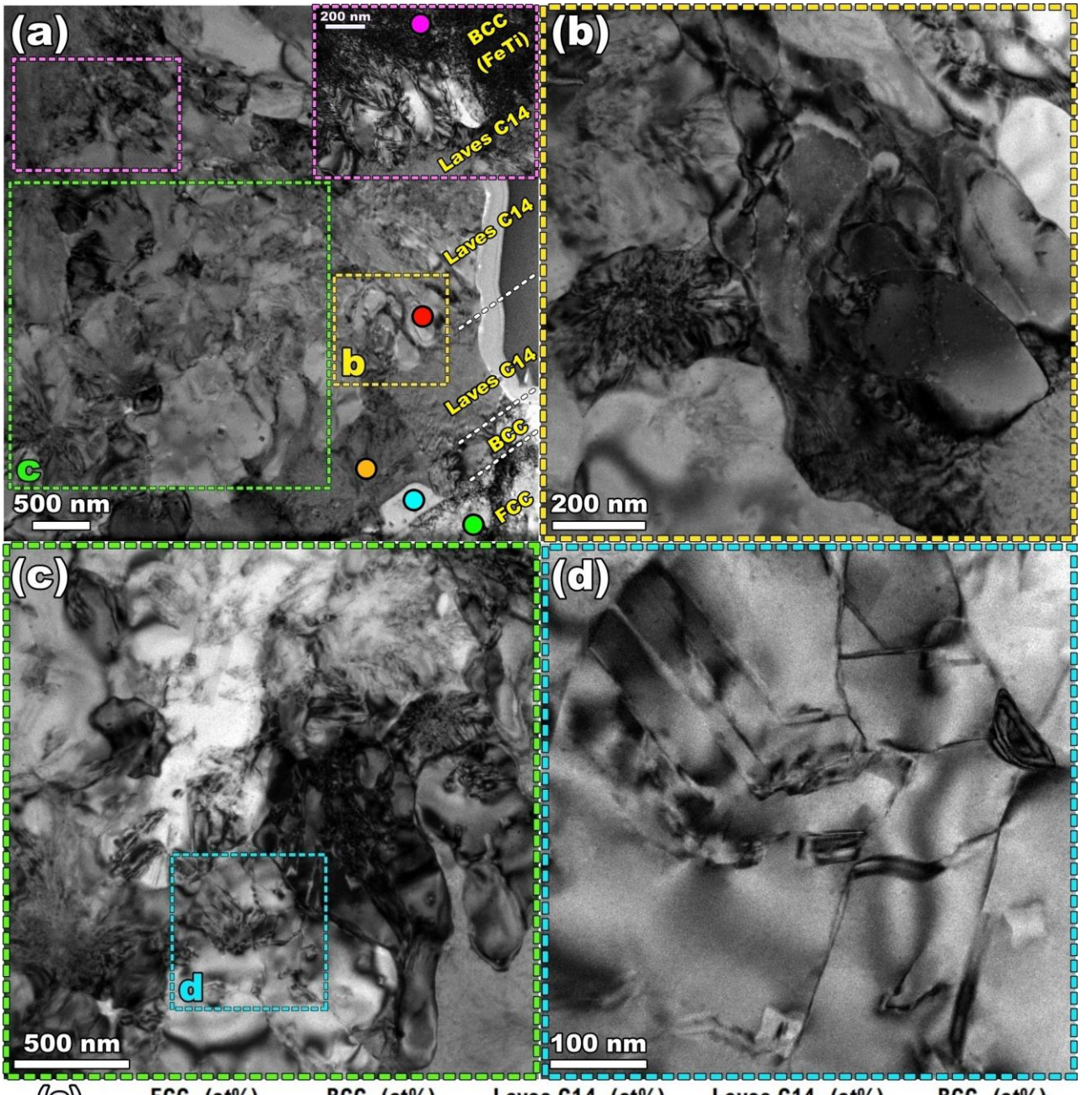

(e) Element	FCC, (at%) Austenite	BCC, (at%) Ferrite	Laves C14, (at%) $Fe_2(Ti,Cr)$	Laves C14, (at%) Fe_2Ti	BCC, (at%) FeTi
Si	0.74	0.67	0.79	0.73	0.28
Ti	0.24	3.93	16.76	23.7	50.7
Cr	19.54	21.95	15.72	13.97	4.84
Mn	3.6	3.06	3.12	2.8	1.39
Fe	62.15	60.31	50.84	48.74	31.89
Ni	12.23	8.35	11.24	8.69	10.37
Mo	1.52	1.74	1.53	1.36	0.52

Fig. 5. TEM images of (a) various phases formed inside a melt-pool, (b) Laves phase, (c, d) the synchroshear phenomenon within the Laves phase, and (e) EDS point analysis acquired from different phases.